Am J Nucl Med Mol Imaging 2014;4(6):548-560
www.ajnmmi.us /ISSN:2160-8407/ajnmmi0001349

Original Article

Intrinsically radiolabelled [^{59}Fe]-SPIONs for dual MRI/radionuclide detection

David Hoffman*, Minghao Sun*, Likun Yang, Philip R McDonagh, Frank Corwin, Gobalakrishnan Sundaresan, Li Wang, Vimalan Vijayaragavan, Celina Thadigiri, Narottam Lamichhane, Jamal Zweit

*Center for Molecular Imaging, Department of Radiology, Virginia Commonwealth University, Richmond, Virginia, 23298, USA. *Equal contributors.*

Received July 8, 2014; Accepted July 25, 2014; Epub September 6, 2014; Published September 15, 2014

Abstract: Towards the development of iron oxide nanoparticles with intrinsically incorporated radionuclides for dual Positron Emission Tomography/Magnetic Resonance Imaging (PET/MRI) and more recently of Single Photon Emission Computed Tomography/Magnetic Resonance Imaging (SPECT/MRI), we have developed intrinsically radiolabeled [^{59}Fe]-superparamagnetic iron oxide nanoparticles ([^{59}Fe]-SPIONs) as a proof of concept for an intrinsic dual probe strategy. ^{59}Fe was incorporated into Fe_3O_4 nanoparticle crystal lattice with 92±3% efficiency in thermal decomposition synthesis. Multidentate poly(acrylic acid)-dopamine-poly(ethylene-glycol-2000) (PAA-DOP-PEG) ligands were designed and synthesized based on facile EDC chemistry and utilized to functionalize the [^{59}Fe]-SPIONs. The transverse relaxivity of [^{59}Fe]-SPIONs (97±3 $s^{-1}mM^{-1}$) was characterized and found to be similar to non-radioactive SPIONs (72±10 $s^{-1}mM^{-1}$), indicating that ^{59}Fe incorporation does not alter the SPIONs' MRI contrast properties. [^{59}Fe]-SPIONs were used to evaluate the nanoparticle biodistribution by *ex vivo* gamma counting and MRI. Nude mice (n=15) were injected with [^{59}Fe]-SPIONs and imaged at various time points with 7T small animal MRI scanner. *Ex vivo* biodistribution was evaluated by tissue-based gamma counting. MRI signal contrast qualitatively correlates with the %ID/g of [^{59}Fe]-SPIONs, with high contrast in liver (45±6%), medium contrast in kidneys (21±5%), and low contrast in brain (4±6%) at 24 hours. This work demonstrates the synthesis and *in vivo* application of intrinsically radiolabeled [^{59}Fe]-SPIONs for bimodal detection and provides a proof of concept for incorporation of both gamma- and positron-emitting inorganic radionuclides into the core of metal based MRI contrast agent nanoparticles.

Keywords: Superparamagnetic iron oxide nanoparticles, intrinsic radiolabeling, biodistribution, PET/MRI, SPECT/MRI, molecular imaging, bimodal detection

Introduction

Recent development of hybrid Positron Emission Tomography/Magnetic Resonance Imaging (PET/MRI) and more recently of Single Photon Emission Computed Tomography/Magnetic Resonance Imaging (SPECT/MRI) systems has not yet been paralleled with the development of a truly hybrid intrinsic PET/MRI probe [1, 2]. In this work, we have developed a method to synthesize a nanoparticle probe that intrinsically incorporates a radionuclide for dual MRI/radionuclide detection. This synthetic method is appropriate for the incorporation of positron- and single photon-emitting radionuclides for future hybrid PET/MRI and SPECT/MRI imaging. This probe brings to molecular imaging a single imaging agent that is detectable by gamma-/positron- emission and MRI, combining therefore, the complementary strengths of each modality.

Superparamagnetic iron oxide nanoparticles (SPIONs) are established MRI contrast agents because of their magnetic properties and low biological toxicity [3-7]. Their surface chemistry has been well characterized and a number of moieties may be used to direct the nanoparticles for targeted molecular imaging and drug delivery [8-10]. First generation clinical SPIONs contrast agents, such as Feridex, Resovist, Lumirem, and Sinerem are produced through co-precipitation of ferrous and ferric iron salts in the presence of carbohydrates to yield dextran or carboxyl-dextran coated particles of varying size [11, 12]. These particles are administered

orally to image the gastrointestinal tract and intravenously to detect lymph node and liver lesions.

In vivo studies in live subjects are essential in order to comprehensively understand the pharmacokinetic and toxicity profiles of these and other nanoparticles towards wider clinical use [13-15]. In order to address this issue, strategies have been developed to synthesize bimodal SPIONs employing surface labeling of radioactive [9, 16, 17] and fluorescent labels [18, 19]. External attachments to the SPIONs surface with imaging labels could alter the pharmacokinetics of the nanoparticles or dissociate from the nanoparticles *in vivo*. Either of these potentialities would affect the quantitative characterization of the SPIONs. Furthermore, fluorescent labeling is limited to qualitative studies, and poor signal penetration is still a problem for deep tissue fluorescence imaging.

A previous study has incubated SPIONs with ^{59}Fe at room temperature to achieve radiolabeled SPIONs encapsulated with amphiphilic polymer or incorporated into lipid micelles [20]. It is not clear from this report whether ^{59}Fe labels the core or the surface of the SPIONs. The claimed core labeling was not substantiated by further experiments such as ligand exchange reaction. Furthermore, this room temperature reaction requires at least 24 hours for moderate ^{59}Fe incorporation yield; this time window may be not compatible with the half-lives of some imaging radionuclides.

A more recent publication has utilized germanium-69 (^{69}Ge) to intrinsically radiolabel SPIONs [21]. The facile radio-labeling reaction with high reaction yield was performed based on the strong absorption of germanium on the SPIONs surface. The PEGylation was introduced to further enhance *in vivo* stability of radiolabeled [^{69}Ge]-SPIONs and *in vivo* PET/MR imaging was demonstrated using this dual-modal nanoprobe.

Towards the development of multi-functional and multi-modal imaging probes, we have previously reported on the intrinsic incorporation of radionuclides into various nanoparticles [22-24]. In this study, we developed a thermal decomposition strategy to incorporate radionuclides into the crystal lattice of SPIONs and this is exemplified by intrinsically radiolabeled [^{59}Fe]-SPIONs. To the best of our knowledge, this is the first description of intrinsic radiolabeling of SPIONs using high temperature organometallic synthesis. This strategy affords high incorporation efficiency in a short time, which is compatible with incorporation of short half-life PET and SPECT radionuclides. The surface modification of [^{59}Fe]-SPIONs was achieved using a multidentate PEGylated ligands to improve SPIONs stability *in vitro* and more importantly in an *in vivo* environment. The biodistribution of this intrinsically radiolabeled [^{59}Fe]-SPIONs was investigated by both *in vivo* MRI as well as *ex vivo* gamma counting. Here we demonstrate the proof of concept of intrinsically radiolabeled nanoparticles for incorporation of PET/SPECT radionuclides for hybrid PET/MRI and SPECT/MRI imaging.

Materials and methods

Chemicals

All chemicals were used as received without further purification. Iron (III) acetylacetonate ($Fe(acac)_3$, 99.9%), 1,2-hexadecanediol (technical grade, 90%), benzyl ether (98%), oleylamine (technical grade, 70%), poly(ethylene-glycol) methyl ether (Mw≈2,000), dopamine•HCl (98%), N-hydroxysuccinimide (NHS, 98%), poly-(acrylic acid) (PAA, Mw=1,800), N-(3-dimethylaminopropyl)-N'-ethylcarbodiimide hydrochloride (EDC, 98%) were purchased from Sigma-Aldrich. Oleic acid (technical grade, 90%) and poly(ethylene-glycol)-2000 (PEG) were obtained from Alfa Aesar. [^{59}Fe]-Fe (III) chloride (half-life=44.5 days, specific activity=24 mCi/mg) was purchased from Perkin Elmer.

Nanoparticles characterization

Transmission electron microscope (TEM) images were recorded on JEOL JEM-1230 operating at an accelerating voltage of 120 KV. The samples were prepared by dropping a diluted solution of SPIONs in toluene on carbon films supported on copper grids (Formvar/Carbon 300 Mesh Cu). These images were processed and the nanoparticle size was evaluated using ImageJ, an open source Java-written program developed by the National Institute of Health for image analysis. Zeta Sizer Nano Series ZEN3600 was used to measure the hydrodynamic size (HD size) and zeta potential of [^{59}Fe]-SPIONs in water. Gamma counter (LKB Wallac 1282 compugamma CS universal gamma counter/Perkin Elmer) was calibrated for ^{59}Fe, resulting in a counting efficiency of 15.2±0.2%

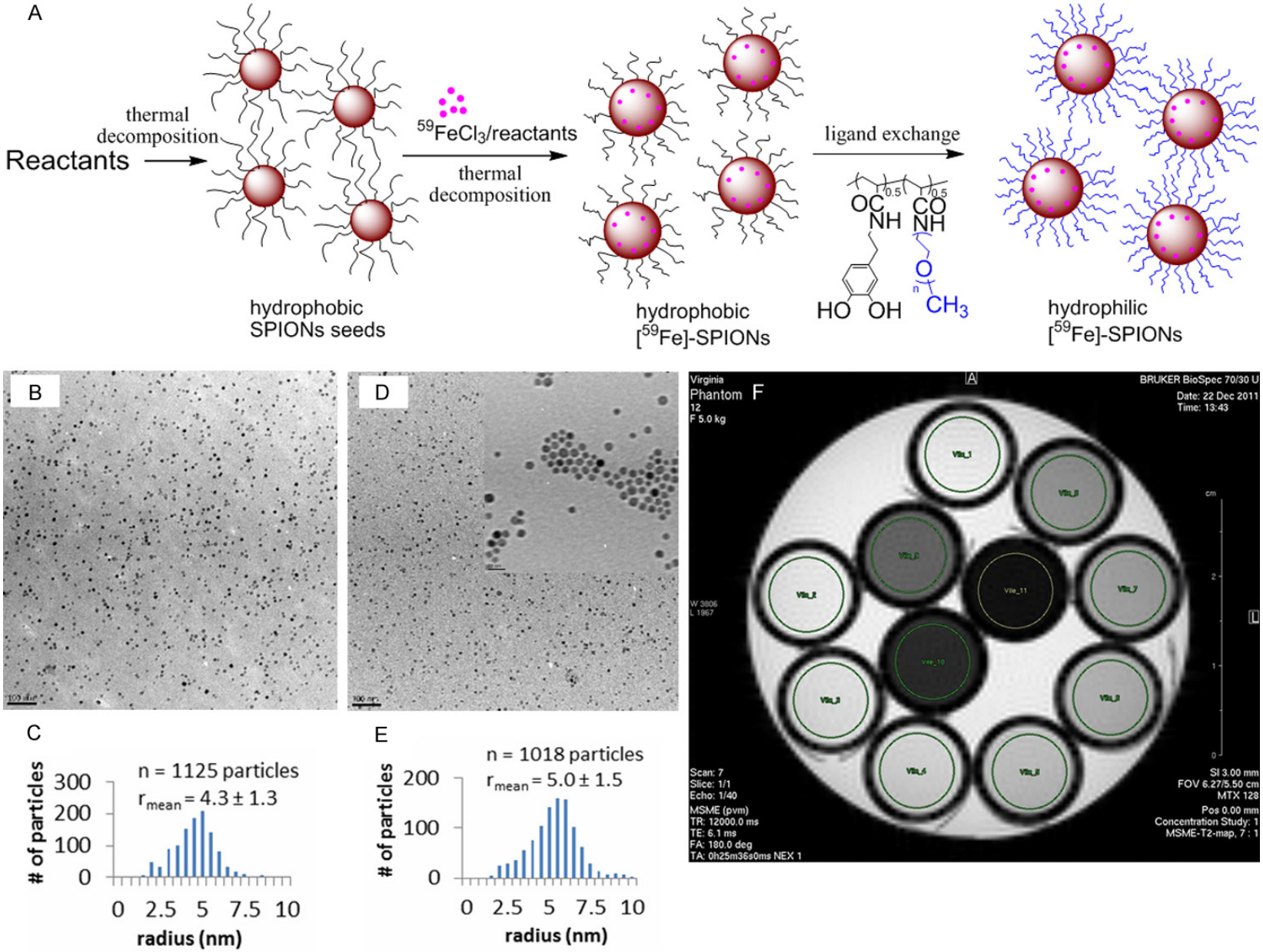
A
thermal decomposition
Reactants
hydrophobic SPIONs seeds
$^{59}FeCl_3$/reactants
thermal decomposition
hydrophobic [^{59}Fe]-SPIONs
ligand exchange
hydrophilic [^{59}Fe]-SPIONs
B
D
C
n = 1125 particles
r_{mean} = 4.3 ± 1.3
# of particles
radius (nm)
E
n = 1018 particles
r_{mean} = 5.0 ± 1.5
# of particles
radius (nm)
F
Virginia
Phantom
BRUKER BioSpec 70/30 U
Date: 22 Dec 2011
Time: 13:43

Figure 1. (A) Synthetic strategy of multidentate PAA-DOP-PEG coated [^{59}Fe]-SPIONs. (B) TEM image and (C) histogram of non-radioactive SPIONs. (D) TEM image and (E) histogram of [^{59}Fe]-SPIONs. Both of the two histogram images were analyzed using ImageJ software. (F) MRI phantom image for [^{59}Fe]-SPIONs with eleven concentrations of Fe: 0, 0.51, 1.15, 2.28, 4.69, 6.89, 9.32, 10.87, 23.40, 46.44, 69.3 mg/L. Note that the scale bar for (B) and (D) is 100 nm. The scale bar of the image insert in (D) is 20 nm.

Table 1. Biodistribution of intravenously injected [^{59}Fe]-SPIONs in nude mice (n=3 per time point). Data are presented as %ID/g (mean±SD) values determined through gamma counting. Data for $^{59}FeCl_3$ at 144 hours is also included for comparison

Organs	1 Hour	4 Hour	24 Hours	72 Hours	144 Hours	144 Hours ($^{59}FeCl_3$)
Blood	3.9±0.7	1.4±0.3	2.8±0.2	4±0.4	5.5±0.7	28±4
Heart	1.2±0.2	0.48±0.07	0.51±0.02	0.8±0.3	0.9±0.2	4.1±0.5
Lungs	1.9±0.5	0.94±0.04	1.2±0.2	1.3±0.4	1.8±0.2	11±3
Liver	46±7	30±7	39±3	33±5	31±2	50±10
Spleen	16±6	19±2	17.5±0.9	14±5	15.2±0.3	48±9
Stomach	0.4±0.3	0.13±0.04	0.25±0.05	0.2±0.2	0.26±0.1	1.1±0.5
Intestines	0.7±0.2	0.9±0.1	1.4±0.1	1.3±0.4	0.8±0.1	2.1±0.8
Kidneys	1.4±0.2	0.7±0.1	0.99±0.1	0.7±0.2	1.4±0.2	6.1±0.7
Skin	0.9±0.4	0.5±0.2	0.7±0.1	0.9±0.2	0.81±0.03	3.4±1
Muscle	0.9±0.6	0.3±0.3	0.19±0.07	0.3±0.3	0.36±0.07	1±0.2
Skull	2.1±0.9	1.8±0.3	1.5±0.4	2.1±0.4	4±1	10±4
Brain	0.14±0.05	0.1±0.1	0.12±0.03	0.12±0.01	0.28±0.08	1.13±0.1
Femur	5.4±0.5	4.9±0.9	7±2	5.3±0.9	4±1	10±2

using both the 1099 keV and 1292 keV gamma-ray energy peaks. ^{1}H NMR spectra were recorded on Varian Mercury 300 spectrometer with solvent proton resonance as reference.

Synthesis of SPIONs seeds and [^{59}Fe]-SPIONs

The first step of the synthesis is to prepare non-radioactive SPIONs seeds using previously reported methods [25, 26] with slight modification, as shown in **Figure 1A**. Briefly, $Fe(acac)_3$ (140 mg, 0.4 mmol), 1,2-hexadecanediol (516.88 mg, 2.0 mmol), benzyl ether (4 mL), oleylamine (395 μL, 1.2 mmol) and oleic acid (380 μL, 1.2 mmol), were loaded into a 25 mL three-neck flask. The reaction was performed under argon flow. The reaction mixture was first heated to 200°C for 2 hours, followed by heating at 300°C for 1 hour. The reaction was cooled down to room temperature after removing the heat source. 50 mL of ethanol was used to precipitate the SPIONs. The SPIONs were dispersed in 5 mL chloroform after centrifugation at 6000 rpm for 5 minutes. In order to remove the undissolved residue, a second centrifugation was applied. The supernatant was then filtrated through 0.2 μm nylon syringe filter to remove larger nanoparticles.

All radioactive experiments were performed in designated lead shield fume hood. All safety measures were taken during handling the radionuclide, including wearing protective clothing and gloves of appropriate radiation shielding. Radioactive contamination was monitored by both external radiation detection as well as swipe testing. The radioactive ^{59}Fe waste was stored in the lead containers and safely stored in designated areas before submitting to the VCU Radiation Safety Office for waste disposal. Radioactive samples submitted for TEM and DLS analysis were monitored and the level of radioactivity in these samples was in the range of 1 to 5 nCi. After measurement, samples were recovered and stored along with the rest of the ^{59}Fe waste.

The second step is to incorporate the radionuclide into the above synthesized SPIONs seeds. $^{59}FeCl_3$ aqueous solution (400 μCi, 100 μL) was transferred to a 25 mL three-neck flask. Argon flow was used to dry the aqueous solution slowly under mild stirring and heating. $Fe(acac)_3$ (20 mg, 0.057 mmol), 1,2-hexadecanediol (516.88 mg, 2 mmol), benzyl ether (4 mL), oleylamine (150 μL, 0.46 mmol) and oleic acid (150 μL, 0.46 mmol) were then added to the flask. The

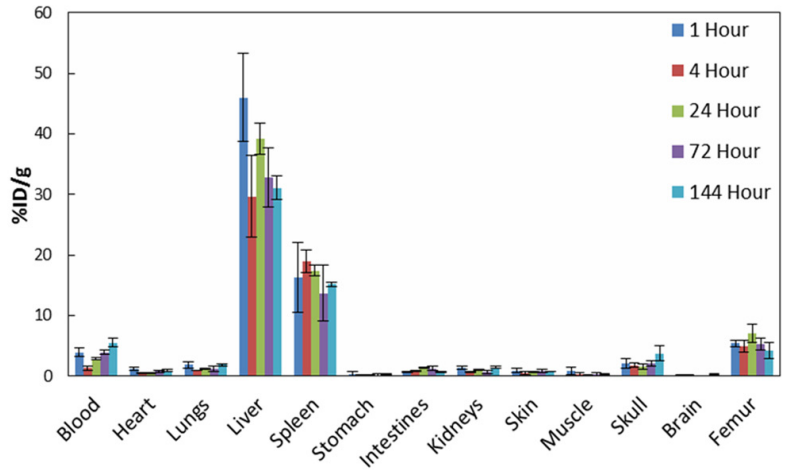

Figure 2. Biodistribution (%ID/g) at various time points post intravenous administration. Nude mice (n=3 per time point) were injected through the tail vein with [^{59}Fe]-SPIONs (26±1 μg Fe, 0.84±0.03 μCi, 200 μL).

non-radioactive SPIONs seeds (12 mg of Fe, 1.7 mL) were loaded and the chloroform was removed under vacuum and heating. The reaction mixture was heated to 200°C for 1 hour, followed by heating to 300°C for 30 minutes under refluxing. After cooling to room temperature, the radioactive [^{59}Fe]-SPIONs were precipitated with the addition of 50 mL of ethanol. The pellet was collected by centrifugation and [^{59}Fe]-SPIONs were re-dissolved in chloroform. The radiolabeling reaction efficiency of ^{59}Fe incorporation was determined by gamma counting.

Synthesis of PAA-dopamine-poly(ethylene-glycol)-2000 (PAA-DOP-PEG) ligands

Amino-PEG-2000 was synthesized as previously described [27, 28]. To a solution of PAA (100 mg, 55.6 μmol) in anhydrous DMSO (3 mL) was added EDC (319 mg, 1.6 mmol) and NHS (192 mg, 1.7 mmol). The reaction solution was stirred at room temperature for 4 hours. Dopamine•HCl (131.6 mg, 0.86 mmol) and N-terminal amino-PEG-2000 (1.4 g, 0.7 mmol) was then added to the solution and kept at room temperature overnight. The solution was then dialyzed against DI water. PAA-DOP-PEG was obtained as white solid (1.4 g, reaction yield 86%). ^{1}H NMR (300 MHz, D_2O, ppm): δ 6.9-6.7 (broad), 3.7 (broad), 3.4 (broad), 3.2-3.1 (broad), 2.9 (broad), 2.8 (broad), 2.7 (broad), 1.9 (broad), 1.1 (broad).

Ligand exchange reaction

Oleylamine/oleic acid coated [^{59}Fe]-SPIONs in chloroform (6 nmole, 2 mL) were mixed with an excess of PAA-DOP-PEG ligands in DI water (5 mmol, 0.5 mL). The mixture was rigorously stirred and heated to 60°C for 30 minutes. Ethyl acetate/hexane (1/1) was then added to precipitate the nanoparticles. The water-soluble [^{59}Fe]-SPIONs pellet was collected and dried under argon flow then dispersed in DI water. The solution of [^{59}Fe]-SPIONs was filtered through a 0.2 μm nylon filter, and purified by a 30 k MW cut off filter (Amicon filters) at 12,000 rpm for 30 minutes. The [^{59}Fe]-SPIONs were collected and diluted in DI water.

Inductively coupled plasma (ICP) measurements

In order to determine relaxometry and mass of Fe in the administered [^{59}Fe]-SPIONs injectate, Fe concentration of [^{59}Fe]-SPIONs solution was measured with ICP atomic emission spectroscopy with a Vista-MPX CCD Simultaneous ICP-OES (Varian). Standards of Fe solutions were used to find the characteristic wavelength at 238.2 nm, and to construct a calibration standard curve. Prior to ICP analysis, samples were digested for 3 days using a 7% nitric acid solution.

MRI phantom studies

Phantom studies were carried out in order to quantify the transverse relaxivity (r_2) induced by [^{59}Fe]-SPIONs. A phantom was made with a 250 mL plastic bottle filled with DI water and containing eleven 2 mL glass vials. Each vial contained a known Fe concentration of [^{59}Fe]-SPIONs for 0, 0.51, 1.15, 2.28, 4.69, 6.89, 9.32, 10.87, 23.40, 46.44, 69.3 mg/L. The [^{59}Fe]-SPIONs solutions were loaded into 2 mL glass vials, avoiding air bubbles. The phantom was imaged in the 7T BioSpec 70/30 small animal MRI scanner (Bruker, Billerica, MA), with a multiple-slice multiple-echo (MSME) sequence where the echoes are acquired at echo times

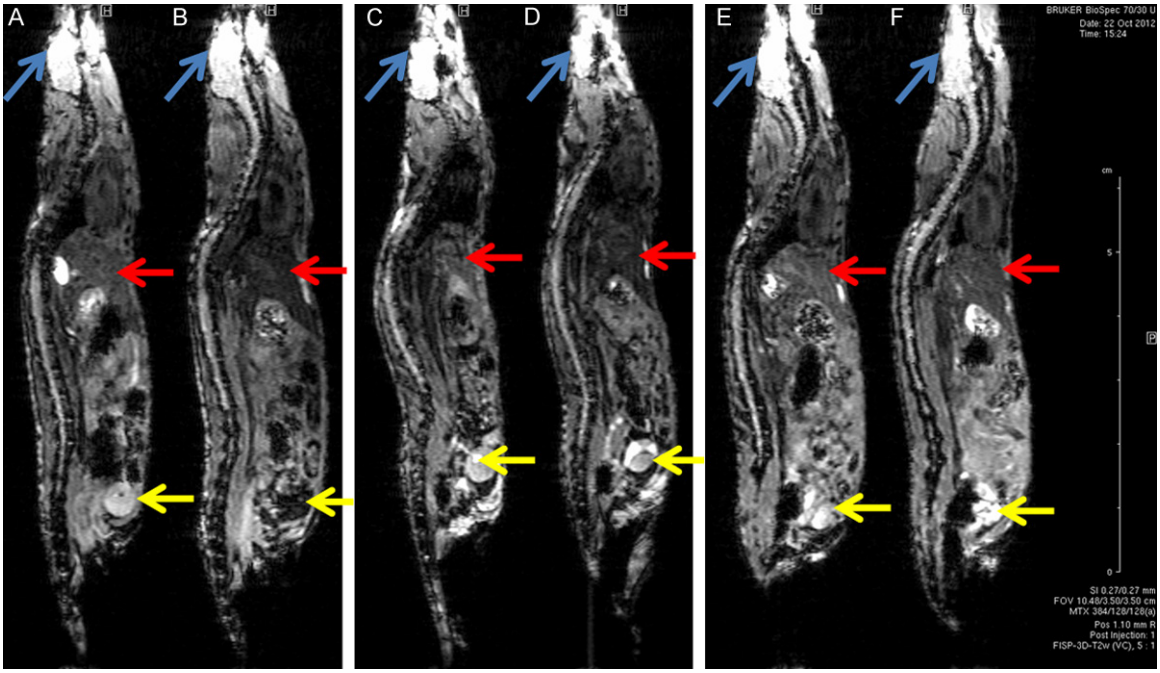

Figure 3. Sagittal MR images of [^{59}Fe]-SPIONs (26±1 μg Fe, 0.84±0.03 μCi). (A, C, E) are baseline scans before [^{59}Fe]-SPIONs injection. (B, D, F) are post injection scans at 1, 24,144 hours respectively. The blue arrows indicate the brain, the red arrows indicate the liver and the yellow arrows indicate the bladder.

(TE) ranging from 10 ms to 640 ms in 10 ms increments, and a repetition time (TR) of 12,000 ms. This produces 64 images of one slice of the phantom at 64 different TEs. The signal intensity from each slice decreases with longer TEs at a rate defined by the transverse relaxivity (T_2). By plotting the signal intensity of a region of interest (ROI) within each vial vs TE, the rate of signal loss was fitted and T_2 was calculated. The effect of the contrast agent on the water of each vial is described using transverse relaxation rates (R_2) rather than times (T_2), which have an inverse relationship, as shown in **Equation 1**.

1. $R_2=1/T_2$

Relaxation rates are additive, so the relaxation rate observed in a vial (R') is the sum of the water's relaxation rate (R) and the relaxation induced by the SPIONs (R_{SPIONs}), as shown in **Equation 2**.

2. $R'=R+R_{SPIONs}$

Within the range of concentrations useful for MR imaging, the relaxation induced by the SPIONs is directly proportional to the concentration of the SPIONs (C) and the SPIONs' specific relaxivity (r_2), as depicted in **Equation 3**.

3. $R_{SPIONs}=r_2C$

By combining equations 1, 2, and 3, it is possible to define the r_2 of a SPIONs sample in terms of the T_2 of a contrast free vial of water (T_{2water}), the measured T_2 of a contrast loaded vial (T_{2vial}), and the known SPIONs concentration (C) within that vial.

4. $r_2=(1/T_{2vial}-1/T_{2water})/C$

Using the T_2 of the SPIONs loaded vials (ms), the T_2 of the non-SPIONs vial (ms), and the SPIONs concentrations (mM of Fe), the r_2 of each vial was calculated using **Equation 4** (1/mM*s). The mean of all of the SPIONs loaded vials was used as the relaxivity value and the standard deviation of the measurements was used to evaluate the uncertainty within the experimental concentration range.

Biodistribution

Animal experiments were approved and performed according to the policies and guidelines of the Animal Care and Use Committee (IACUC) at Virginia Commonwealth University. Adult male and female nude mice (Harlan, USA) were injected, with the solution of PEGylated [^{59}Fe]-SPIONs in saline (26±1 μg Fe, 0.84±0.03 μCi,

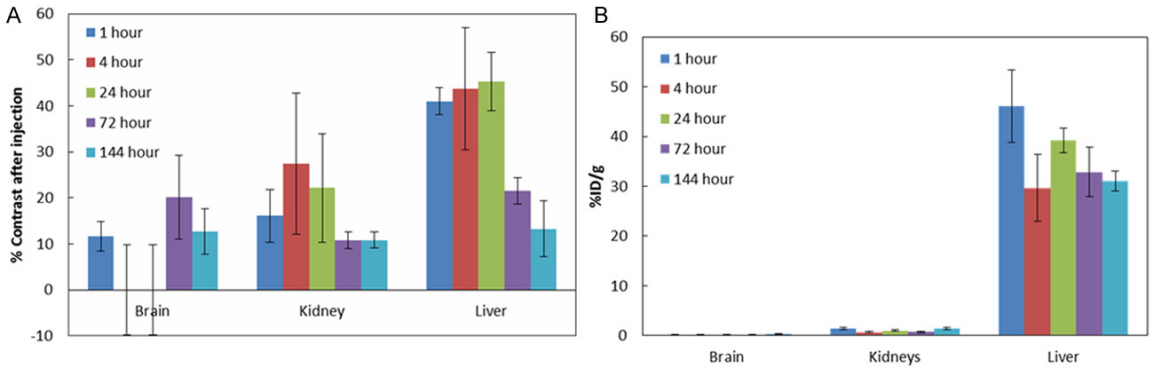

Figure 4. (A) The MRI contrast caused by the [^{59}Fe]-SPIONs injection as measured by ROI analysis of various tissues and (B) the %ID/g of those tissues from biodistribution for comparison (n=3 per time point).

200 μL), through the tail vein. Mice were euthanized and blood samples and major organs were harvested and weighed at different time points after injection (1, 4, 24, 72, 144 hours; n=3 per time point). Radioactivity of each sample including injection standards were measured by gamma counter and the percentage of the injected dose per gram (%ID/g) of tissues were calculated.

MR animal imaging

In order to validate the dual MR/nuclear probe concept, both *in vivo* MR imaging and *ex vivo* gamma counting were performed on the same animals. This enabled the correlation between *ex vivo* ^{59}Fe data with ROI analysis of *in vivo* MRI data. A Fast Imaging with Steady State Precession (FISP) sequence was used with a TR of 9.4 ms and TE of 4.7 ms. A total of 4 acquisitions were performed. A flip angle (FA) of 35° was used to achieve T2*/T1 weighted images. The short TR (9.4 ms) allowed for a 384×128×128 matrix acquisition with isotropic 274 micron voxels (FOV=10.5×3.5×3.5 cm). The isotropic acquisition was specifically developed to allow for future comparison with isotropic PET data. Attenuator and receiver gain values were recorded from the pre-injection imaging and reused for the pre-sacrifice imaging. The ungated acquisition time was 614 s. A pneumatic pillow sensor placed under the mouse chest and connected through an ERT Control/Gating Module (SA Instruments) was used to acquire the mouse's respiratory cycle. The MRI sequence was actively gated to avoid acquisition during inhalation and exhalation. This gating increased the acquisition time to ~13 minutes. The mice were anesthetized under 2% isoflurane flow during imaging. The images were exported in Digital Imaging and Communications in Medicine (DICOM) format for processing and analysis using the 3D Slicer software package.

Additionally, the phantom described in phantom study section was imaged using the same sequence parameters to produce a % contrast vs [^{59}Fe]-SPIONs concentration standard curve. ROIs were drawn on the brain, kidneys, and liver of each mouse before and after injection to quantify the % contrast caused by the [^{59}Fe]-SPIONs injection at different time points. These % contrast values were then used to calculate probe concentrations based on the % contrast vs [^{59}Fe]-SPIONs concentration standard curve. These MRI derived probe concentrations were then compared to radionuclide probe concentrations.

Results

Synthesis, surface functionalization and characterization of [^{59}Fe]-SPIONs

[^{59}Fe]-SPIONs were synthesized through thermal decomposition of organometallic complexes, as shown in **Figure 1A**. The regular crystallinity of [^{59}Fe]-SPIONs from thermal decomposition synthesis results in high paramagnetic properties and a high ^{59}Fe radiolabeling reaction yield (92±3%). The radius of the non-radioactive SPIONs, measured by TEM, was 4.3±1.3 nm before radionuclide incorporation (**Figure 1B** and **1C**) and grew to 5.0±1.5 nm after radionuclide incorporation (**Figure 1D** and **1E**). Following ligand exchange with PAA-DOP-PEG, the HD size of [^{59}Fe]-SPIONs increased to 17±6

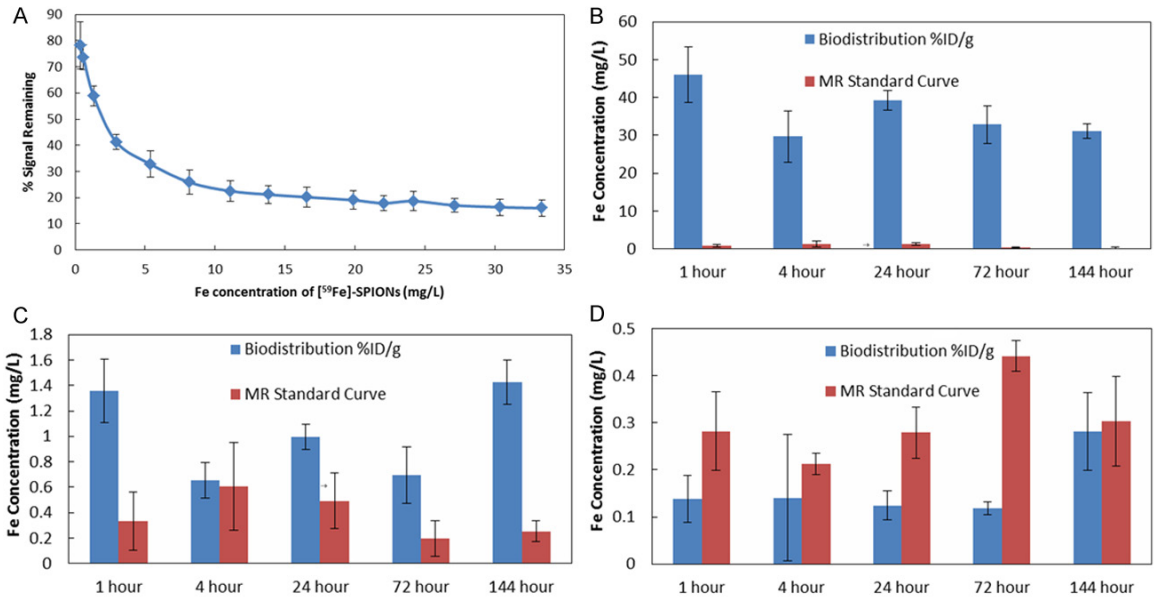

Figure 5. (A) The standard curve of % signal remaining vs Fe concentration of [^{59}Fe]-SPIONs. The connecting line segments represent the linear interpolation used to evaluate values between the known concentrations. Fe concentrations are calculated from MRI ROI % contrast data and [^{59}Fe]-SPIONs biodistribution %ID/g values for (B) liver, (C) kidneys and (D) brain (n=3 per time point).

nm. The zeta potential of water-soluble [^{59}Fe]-SPIONs was -46±5 mV. The transverse relaxivity (r_2) of [^{59}Fe]-SPIONs was 97±3 $mM^{-1}sec^{-1}$, as measured in the MRI phantom study (**Figure 1F**). As a comparison, a fraction of the non-radioactive SPIONs seeds produced in the first step of the synthesis were coated with the same ligands, and the transverse relaxivity of these SPIONs was 72±10 $mM^{-1}sec^{-1}$. The slight increase in relaxivity of [^{59}Fe]-SPIONs, compared with non-radioactive SPIONs, could be attributed to the quadruple nature of ^{59}Fe nuclei (^{59}Fe nuclear spin, I=3/2 vs 0 for ^{56}Fe).

Biodistribution

The %ID/g of [^{59}Fe]-SPIONs in blood and major organs, at different time points after injection, was measured by ^{59}Fe gamma counting, as shown in **Table 1** and **Figure 2**. Consistent with nanoparticle pharmacokinetics, the [^{59}Fe]-SPIONs biodistribution exhibited large accumulation in the liver and spleen due to scavenging and phagocytosis by cellular elements of RES. It is also interesting to note a slight increase in the blood %ID/g with time; which could be due to the degradation of ^{59}Fe from the [^{59}Fe]-SPIONs and subsequent incorporation into blood elements. Accumulation in the femur could also be indicative of bone marrow uptake as a result of this.

MR imaging

Representative MR images of [^{59}Fe]-SPIONs injected mice are shown in **Figure 3** for baseline scans and post injection scans at 1, 24 and 144 hours. High contrast was observed in liver, while medium contrast was observed in kidneys, and little or no contrast was observed in brain. ROIs were drawn on these three larger tissues, and the contrast induced by the [^{59}Fe]-SPIONs injection was quantified and compared to the biodistribution data in **Figure 4**.

In an effort to determine Fe concentration from only MRI ROI data (for comparison with radionuclide detection concentration measurements), a standard curve of contrast (% Signal Remaining) vs Fe concentration of [^{59}Fe]-SPIONs (mg/L) was produced in a phantom study and is shown in **Figure 5A**. Concentrations between the known values where linearly interpolated, as shown by the connecting line segments. Fe concentrations calculated from MRI data and biodistribution are shown in **Figure 5B-D**. Fe concentrations calculated at each time point, from MRI data, were greater than the ones calculated from biodistribution by a mean factor

of 62±38 in liver, 3.2±1.8 in kidneys and 0.55±0.25 in brain. This result demonstrates the difficulty of accurately evaluating Fe concentration of [^{59}Fe]-SPIONs solely from MRI data.

Discussion

The co-precipitation synthesis produces polydisperse particles with poor crystallinity, which results in weaker MRI contrast properties [29]. Methods have been developed to produce high quality single-crystalline SPIONs through high temperature decomposition of iron complexes, such as $Fe(Cup)_3$, $Fe(CO)_5$, or $Fe(acac)_3$, in the presence of surfactants and organic solvents [30, 31]. SPIONs with improved magnetization are obtained through a nucleation and growth process with fine reaction control that determines the size, composition and surface properties of the nanoparticles. These hydrophobic magnetic nanoparticles have been made water-soluble and biocompatible through a number of strategies, including ligand exchange against hydrophilic polymers, or through interaction with amphiphilic polymer to form hydrophilic layer [32-34]. The relaxivity of SPIONs depends on the quality of nanoparticle crystal and the surface coating layer. Usually, larger nanoparticles and thinner hydrophilic layer improve the relaxivity of SPIONs for MRI. This is due to the enhanced magnetization of larger nanoparticles and easier access of water molecules to thinly coated SPIONs. Although some reports indicate that the relaxivity can be high, by using amphiphilic lipid-poly(ethylene-glycol) (PEG) modification SPIONs, a facile and efficient surface functionalization could be acquired by ligand exchange of SPIONs with specifically designed ligands [35, 36]. Therefore, the overall synthetic strategy in this study was involved of incorporation of radionuclide into nanocrystal by thermal decomposition reaction and convert hydrophobic nanoparticles to hydrophilic one by ligand exchange with multidentate polymer ligands.

The reaction yield of radio-synthesis of [^{59}Fe]-SPIONs by thermal decomposition reaches to 92±3% from gamma counting. In order to make high quality radioactive [^{59}Fe]-SPIONs with high reaction yield, it is crucial to control the reaction temperature. It was found that the reaction is susceptible to the reaction temperature which is influenced by existence of trace amount water/acid. So completely removal of water/HCl before radiolabeling reaction is important. High specific activity of [^{59}Fe]-$FeCl_3$ is beneficial to the reaction because the existence of chloride ions in the reaction could be potentially influence the quality of [^{59}Fe]-SPIONs. We speculate the [^{59}Fe]-$FeCl_3$ was converted to complex of ^{59}Fe-oleate/olelamine with cold $Fe(acac)_3$ and adsorb on Fe_3O_4 crystal. At high reaction temperature the Fe-complex may further decompose to form Fe_3O_4 crystal and was doped into the crystal lattice of SPIONs.

Dopamine derivatives are efficient ligands for making water-soluble SPIONs [37, 38]. However, the high toxicity of dopamine limits its biological applications. From our previous experience we found that multidentate polymer ligands are good candidates for surface functionalization of nanoparticles because they form tight interaction with nanoparticles [39]. Additionally, the multi-functionality of polymer ligands makes it feasible to introduce various moieties on the surface of SPIONs to afford targeted imaging and/or manipulate the nanoparticle pharmacokinetics. PEGylation is a widely used strategy to make biocompatible nanoparticles [40, 41]. We also adopted this approach to incorporate PEG chains into our ligand design in order to improve water-solubility and PEG-2000 was selected to achieve stability, favorable biodistribution and acceptable relaxivity.

The multidentate PAA-DOP-PEG ligands were synthesized by EDC chemistry and the ratio of DOP/PEG was set as 1/1. The chemical shift of proton from DOP was confirmed from NMR measurement. Strong interaction between DOP and the surface of [^{59}Fe]-SPIONs makes it easy to convert hydrophobic [^{59}Fe]-SPIONs with oleic acid/olelamine coating to hydrophilic nanoparticles efficiently through ligand exchange reaction. It was found that surface functionalization of [^{59}Fe]-SPIONs by multidentate PAA-DOP-PEG ligands did not release the radionuclide from the nanoparticles, which is verified by sample dialysis over 30k MWCO filters after ligand exchange reaction. This reflects good stability of [^{59}Fe]-SPIONs obtained from the intrinsically radiolabeling method. We also synthesized the dopamine-sulfobetaine (DOP-SB) zwitterionic ligands and applied ligand exchange to [^{59}Fe]-SPIONs with DOP-SB. However, the radioactivity was detected from the supernatant after

dialysis [^{59}Fe]-SPIONs against 30K MWCO filters, which reflects the instability of [^{59}Fe]-SPIONs with DOP-SB ligands. Design/synthesis of the appropriate ligands to functionalize [^{59}Fe]-SPIONs are tricky and important to achieve stable paramagnetic nanoparticles with high relaxivity. TEM measured the radius of the inorganic SPIONs increasing from 4.3±1.3 nm to 5.0±1.5 nm with the addition of the shell in the second step of the synthesis. This is likely due to the addition of an iron oxide shell that contains both Fe from $Fe(acac)_3$ monomer and ^{59}Fe from [^{59}Fe]-$FeCl_3$. The slightly increased size of [^{59}Fe]-SPIONs also resulted in the enhanced transverse relaxivity r_2 as 97±3 $(s*mM\ of\ Fe)^{-1}$ vs 72±10 $(s*mM\ of\ Fe)^{-1}$ of non-radioactive SPIONs seeds, indicating that ^{59}Fe incorporation did not reduce the nanoparticles' magnetization and application as a MRI contrast agent. Possible reasons of the improved relaxivity are the increased size and further regulation of crystal lattice of [^{59}Fe]-SPIONs within the second step of synthesis/thermal cycling process. The high relaxometry of PAA-DOP-PEG coated [^{59}Fe]-SPIONs may be also due to the thin hydrophilic surface coating, which allows the water molecules to access [^{59}Fe]-SPIONs. The radio-isotope incorporation, ligand exchange and purification were accomplished within 6-8 hours, which is appropriate for 44.5 days half-life of ^{59}Fe and will be useful for other shorter lived radionuclides.

The intrinsic incorporation method offers advantages compared with extrinsic radiolabeling approaches. The entire surface of the nanoparticles is available for conjugation with targeting molecules, anti-cancer drugs, fluorescent molecules and other moieties. Additionally, the radio-isotope is less likely to become dissociated from the nanoparticles while interacting with biological compartments. While an extrinsic radiolabels may separate from the nanoparticles due to damage to the coating ligands, separation of the intrinsically incorporated radio-isotope would only likely happen if the nanoparticles is being degraded or digested as a whole. Surface functionalization is an important factor for determining the biological behavior of nanoparticles. Compared with monodentate ligands, the multidentate ligands interact with the surface of nanoparticles tightly and improved stability of nanoparticles by reducing the aggregation. We have demonstrated the stability of [^{59}Fe]-SPIONs by incubating with mouse plasma for up to 24 hours without observing any precipitation [data not shown].

[^{59}Fe]-SPIONs have been demonstrated as bimodal nanoprobes by MRI and *ex vivo* gamma counting. At early time points (≤ 24 hours), MRI ROI % contrast and %ID/g qualitatively correlated with high liver, medium kidneys, and low brain uptake, as shown in **Figure 4**. At later time points (≥ 72 hours), the liver MRI ROI % contrast decreased sharply, while ^{59}Fe %ID/g decreased only a small amount. This may indicate that over time, ^{59}Fe is partially retained by liver after [^{59}Fe]-SPIONs was degraded and causing loss of MRI contrast. This possibility is strengthened by the %ID/g increasing in kidneys and blood at 144 hours post injection, which would be characteristic of Fe associated with smaller non-nanoparticle molecules. Enzyme induced degradation of SPIONs in liver was reported previously [42, 43]. It is expected the nanoparticles showed high RES accumulation due to the interaction of nanoparticles with kupffer cells, macrophages and other immune cells. It looks like free ^{59}Fe could be taken up by the red blood cells. Other forms of degraded SPIONs could also exist such as fractions or smaller nanoparticles. The fate of [^{59}Fe]-SPIONs can be quantitatively monitored by radiotracer trafficking. It will be useful to synthesize PET/SPECT isotope SPIONs to monitor the *in vivo* pharmacokinetics/biodistribution by both MRI and radionuclide imaging. It is necessary to point out that the possible *in vivo* degradation of [^{59}Fe]-SPIONs, demonstrated here, may not be due to the radiolabeling method or surface functionalization but rather due to the intrinsic instability of [^{59}Fe]-SPIONs per se.

Fe concentrations, determined in liver, kidneys, and brain from MRI ROIs, did not correlate with values derived from ^{59}Fe gamma emission. This could be due to a number of reasons. For MRI, the image signal is not originating from the nanoparticles, but rather from the hydrogen protons of the imaged tissues. The interaction of those protons with the nanoparticles results in image contrast. Within the biological tissues, this interaction may be changed by a multitude of effects. For example, nanoparticles sequestered in liver may be tightly localized in cellular vesicles, which could reduce their effectiveness as MRI contrast agents. Hence, this

approach is not appropriate for quantitatively measuring Fe concentration from MRI data. The difficulty in quantifying Fe concentration from MRI data alone demonstrated the usefulness of [^{59}Fe]-SPIONs, which can be used to observe spatial distribution with MRI and quantitative biodistribution from gamma emission.

This work is a proof of concept of an intrinsically incorporated radio-isotope into SPIONs for bimodal detection. Future work will incorporate a targeting molecule to the surface of the nanoparticles for targeted molecular imaging. Additional upcoming work will incorporate a PET or SPECT imaging isotope for hybrid PET/MRI or SPECT/MRI contrast. The MRI results of this work indicate the potential usefulness of such a probe. The calculation of Fe concentration from MRI data was unsuccessful, indicating that pairing this probe with a strongly quantitative imaging modality, such as PET, may allow for improved probe concentration measurements. The creation of % signal contrast maps with isotropic 274 micron voxel size from MRI data showed that MRI contrast offers a good image spatial resolution. A hybrid PET/MRI or SPECT/MRI probe has the potential to provide better probe concentration quantification from either PET or SPECT signal, and higher spatial resolution from MRI contrast to create images that offer more relevant biological information than that could be achieved from either imaging modality alone [42-44].

Conclusion

A strategy to synthesize radio-intrinsic [^{59}Fe]-SPIONs has been developed and implemented. The multidentate PAA-DOP-PEG ligands were synthesized and used to acquire biocompatible [^{59}Fe]-SPIONs for *in vivo* study. The intrinsically radiolabeled method provides the stable hybrid nanoprobe, which has both MRI signal as well as gamma emission. We have demonstrated the bimodal detection of this nanoprobe *in vivo* through gamma emission based biodistribution and MRI studies. The MRI data has been used to show nanoparticles uptake that qualitatively corresponds with the biodistribution results. We believe that this combined platform provides the proof of concept for incorporating both PET and SPECT radionuclides for hybrid radionuclide/MRI. Work incorporating both PET and SPECT radionuclides, to further validate this strategy, is underway.

Acknowledgements

This work was funded in part by VCU School of Medicine and the Society of Nuclear Medicine and Molecular Imaging Predoctoral Imaging Research Grant (DH). We acknowledge Dr. Everett. E. Carpenter and Dr. Joseph Turner (Department of Chemistry, Virginia Commonwealth University) for assistance with ICP and DLS measurements.

Disclosure of conflict of interest

None.

Address correspondence to: Dr. Jamal Zweit, Center for Molecular Imaging, Department of Radiology, Virginia Commonwealth University, *8-022, 1101 East Marshall Street,* Richmond, VA, 23298, USA. E-mail: jzweit@vcu.edu

References

[1] Xie J, Chen K, Huang J, Lee S, Wang J, Gao J, Li X, Chen X. PET/NIRF/MRI triple functional iron oxide nanoparticles. Biomaterials 2010; 31: 3016-3022.

[2] Bailey DL, Barthel H, Beuthin-Baumann B, Beyer T, Bisdas S, Boellaard R, Czernin J, Drzezga A, Ernemann U, Franzius C, Gückel B, Handgretinger R, Hartenbach M, Hellwig D, Nadel H, Nekolla SG, Pfluger T, Pichler BJ, Quick HH, Sabri O, Sattler B, Schäfer J, Schick F, Siegel BA, Schlemmer HP, Schwenzer NF, Hoff J, Veit-Haibach P, Wehrl HF. Combined PET/MR: Where Are We Now? Summary Report of the Second International Workshop on PET/MR Imaging April 8-12, 2013, Tubingen, Germany. Mol Imaging Biol 2014; 16: 295-310.

[3] Stark DD, Weissleder R, Elizondo G, Hahn PF, Saini S, Todd LE, Wittenberg J, Ferrucci JT. Superparamagnetic iron oxide: clinical application as a contrast agent for MR imaging of the liver. Radiology 1988; 168: 297-301.

[4] Laurent S, Forge D, Port M, Roch A, Robic C, Vander Elst L, Muller RN. Magnetic iron oxide nanoparticles: synthesis, stabilization, vectorization, physicochemical characterizations, and biological applications. Chem Rev 2008; 108: 2064-2110.

[5] Thorek DLJ, Chen AK, Czupryna J, Tsourkas A. Superparamagnetic iron oxide nanoparticle probes for molecular imaging. Ann Biomed Eng 2006; 34: 23-38.

[6] Liu F, Laurent S, Fattahi H, Elst LV, Muller RN. Superparamagnetic nanosystems based on iron oxide nanoparticles for biomedical imaging. Nanomedicine 2011; 6: 519-528.

[7] Lu AH, Salabas EL, Schüth F. Magnetic nanoparticles: synthesis, protection, functionalization, and application. Angew Chem Int Edit 2007; 46: 1222-1244.
[8] Jain TK, Richey J, Strand M, Leslie-Pelecky DL, Flask CA, Labhasetwar V. Magnetic nanoparticles with dual functional properties: drug delivery and magnetic resonance imaging. Biomaterials 2008; 29: 4012-4021.
[9] Yang X, Hong H, Grailer JJ, Rowland IJ, Javadi A, Hurley SA, Xiao Y, Yang Y, Zhang Y, Nickles RJ, Cai W, Steeber DA, Gong S. cRGD-functionalized, DOX-conjugated, and ^{64}Cu-labeled superparamagnetic iron oxide nanoparticles for targeted anticancer drug delivery and PET/MR imaging. Biomaterials 2011; 32: 4151-4160.
[10] Tong S, Hou S, Zheng Z, Zhou J, Bao G. Coating optimization of superparamagnetic iron oxide nanoparticles for high T2 relaxivity. Nano lett 2010; 10: 4607-4613.
[11] Kopp AF, Laniado M, Dammann F, Stern W, Grönewäller E, Balzer T, Schimpfky C, Claussen CD. MR imaging of the liver with resovist: safety, efficacy, and pharmacodynamic properties. Radiology 1997; 204: 749-756.
[12] Berry I, Benderbous S, Ranjeva J-P, Gracia-Meavilla D, Manelfe C, Le Bihan D. Contribution of Sinerem used as blood-pool contrast agent: detection of cerebral blood volume changes during apnea in the rabbit. Magn Reson Med 1996; 36: 415-419.
[13] Longmire M, Choyke PL, Kobayashi H. Clearance properties of nano-sized particles and molecules as imaging agents: considerations and caveats. Nanomedicine 2008; 3: 703-717.
[14] Choi HS, Liu W, Misra P, Tanaka E, Zimmer JP, Ipe BI, Bawendi MG, Frangioni JV. Renal clearance of quantum dots. Nat Biotechnol 2007; 25: 1165-1170.
[15] Nel A, Xia T, Mädler L, Li N. Toxic potential of materials at the nanolevel. Science 2006; 311: 622-627.
[16] Jalilian AR, Panahifar A, Mahmoudi M, Akhlaghi M, Simchi A. Preparation and biological evaluation of [^{67}Ga]-labeled-superparamagnetic nanoparticles in normal rats. Radiochim Acta 2009; 97: 51-56.
[17] Lee HY, Li Z, Chen K, Hsu AR, Xu C, Xie J, Sun S, Chen X. PET/MRI dual-modality tumor imaging using arginine-glycine-aspartic (RGD)–Conjugated radiolabeled iron oxide nanoparticles. J Nucl Med 2008; 49: 1371-1379.
[18] Lee JH, Schneider B, Jordan EK, Liu W, Frank JA. Synthesis of complexable fluorescent superparamagnetic iron oxide nanoparticles (FL SPIONs) and Cell labeling for clinical application. Adv Mater 2008; 20: 2512-2516.
[19] Mahmoudi M, Shokrgozar MA. Multifunctional stable fluorescent magnetic nanoparticles. Chem Commun 2012; 48: 3957-3959.
[20] Freund B, Tromsdorf UI, Bruns OT, Heine M, Giemsa A, Bartelt A, Salmen SC, Raabe N, Heeren J, Ittrich H, Reimer R, Hohenberg H, Schumacher U, Weller H, Nielsen P. A Simple and widely applicable method to ^{59}Fe-Radiolabel monodisperse superparamagnetic iron oxide nanoparticles for *in vivo* quantification studies. ACS Nano 2012; 6: 7318-7325.
[21] Chakravarty R, Valdovinos HF, Chen F, Lewis CM, Ellison PA, Luo H, Meyerand ME, Nickles RJ, Cai W. Intrinsically Germanium-69-labeled iron oxide nanoparticles: synthesis and in vivo dual-modality PET/MR imaging. Adv Mater 2014; 26: 5119-23.
[22] Yang L, Sundaresan G, Sun M, Jose P, Hoffman D, McDonagh PR, Lamichhane N, Cutler CS, Perez JM, Zweit J. Intrinsically radiolabeled multifunctional cerium oxide nanoparticles for *in vivo* studies. J Mater Chem B 2013; 1: 1421-1431.
[23] Sun M, Hoffman D, Sundaresan G, Yang L, Lamichhane N, Zweit J. Synthesis and characterization of intrinsically radiolabeled quantum dots for bimodal detection. Am J Nucl Med Mol Imaging 2012; 2: 122-135.
[24] Sun M, Sundaresan G, Jose P, Yang L, Hoffman D, Lamichhane N, Zweit J. Highly stable intrinsically radiolabeled indium-111 quantum dots with multidentate zwitterionic surface coating: dual modality tool for biological imaging. J Mater Chem B 2014; 2: 4456-4466.
[25] Sun S, Zeng H, Robinson DB, Raoux S, Rice PM, Wang SX, Li G. Monodisperse MFe_2O_4 (M = Fe, Co, Mn) nanoparticles. J Am Chem Soc 2004; 126: 273-279.
[26] Xie J, Peng S, Brower N, Pourmand N, Wang SX, Sun S. One-pot synthesis of monodisperse iron oxide nanoparticles for potential biomedical applications. Pure Appl Chem 2006; 78.
[27] Na HB, Palui G, Rosenberg JT, Ji X, Grant SC, Mattoussi H. Multidentate catechol-based polyethylene glycol oligomers provide enhanced stability and biocompatibility to iron oxide nanoparticles. ACS Nano 2012; 6: 389-399.
[28] Krpetić Ž, Nativo P, Porta F, Brust M. A multidentate peptide for stabilization and facile bioconjugation of gold nanoparticles. Bioconjugate Chem 2009; 20: 619-624.
[29] Na HB, Song IC, Hyeon T. Inorganic nanoparticles for MRI contrast agents. Adv Mater 2009; 21: 2133-2148.
[30] Sun S, Zeng H. Size-controlled synthesis of magnetite nanoparticles. J Am Chem Soc 2002; 124: 8204-8205.
[31] Hyeon T, Lee SS, Park J, Chung Y, Na HB. Synthesis of highly crystalline and monodisperse maghemite nanocrystallites without a size-se-

lection process. J Am Chem Soc 2001; 123: 12798-12801.
[32] Sun C, Lee JSH, Zhang M. Magnetic nanoparticles in MR imaging and drug delivery. Adv Drug Deliver Rev 2008; 60: 1252-1265.
[33] Kohler N, Sun C, Fichtenholtz A, Gunn J, Fang C, Zhang M. Methotrexate-immobilized poly (ethylene glycol) magnetic nanoparticles for MR imaging and drug delivery. Small 2006; 2: 785-792.
[34] Yu WW, Chang E, Sayes CM, Drezek R, Colvin VL. Aqueous dispersion of monodisperse magnetic iron oxide nanocrystals through phase transfer. Nanotechnology 2006; 17.
[35] Lartigue L, Innocenti C, Kalaivani T, Awwad A, Sanchez Duque MdM, Guari Y, Larionova J, Guérin C, Montero JLG, Barragan-Montero V, Arosio P, Lascialfari A, Gatteschi D, Sangregorio C. Water-dispersible sugar-coated iron oxide nanoparticles. An evaluation of their relaxometric and magnetic hyperthermia properties. J Am Chem Soc 2011; 133: 10459-10472.
[36] Wei H, Bruns OT, Chen O, Bawendi MG. Compact zwitterion-coated iron oxide nanoparticles for *in vitro* and *in vivo* imaging. Integr Biol (Camb) 2013; 5: 108-14.
[37] Xie J, Xu C, Kohler N, Hou Y, Sun S. Controlled PEGylation of monodisperse Fe_3O_4 nanoparticles for reduced non-specific uptake by macrophage cells. Adv Mater 2007; 19: 3163-3166.
[38] Xie J, Chen K, Lee HY, Xu C, Hsu AR, Peng S, Chen X, Sun S. Ultrasmall c(RGDyK)-coated Fe_3O_4 nanoparticles and their specific targeting to integrin αvβ3-rich tumor cells. J Am Chem Soc 2008; 130: 7542-7543.
[39] Sun M, Yang L, Jose P, Wang L, Zweit J. Functionalization of quantum dots with multidentate zwitterionic ligands: impact on cellular interactions and cytotoxicity. J Mater Chem B 2013; 1: 6137-6146.
[40] Uyeda HT, Medintz IL, Jaiswal JK, Simon SM, Mattoussi H. Synthesis of compact multidentate ligands to prepare stable hydrophilic quantum dot fluorophores. J Am Chem Soc 2005; 127: 3870-3878.
[41] Choi HS, Ipe BI, Misra P, Lee JH, Bawendi MG, Frangioni JV. Tissue- and organ-selective biodistribution of NIR fuorescent quantum dots. Nano Lett 2009; 9: 2354-2359.
[42] Briley-Saebo K, Bjornerud A, Grant D, Ahlstrom H, Berg T, Kindberg GM. Hepatic cellular distribution and degradation of iron oxide nanoparticles following single intravenous injection in rats: implications for magnetic resonance imaging. Cell Tissue Res 2004; 316: 315-323.
[43] Jain TK, Reddy MK, Morales MA, Leslie-Pelecky DL, Labhasetwar V. Biodistribution, clearance and biocompatibility of iron oxide nanoparticles in rats. Mol Pharm 2008; 5: 316-327.
[44] Pichler BJ, Judenhofer MS, Catana C, Walton JH, Kneilling M, Nutt RE, Siegel SB, Claussen CD, Cherry SR. Performance test of an LSO-APD detector in a 7-T MRI scanner for simultaneous PET/MRI. J Nucl Med 2006; 47: 639-647.